

RESEARCH ARTICLE

10.1002/2015JB011886

Key Points:

- We present a new method to mitigate atmospheric phase delays in InSAR data
- We apply the method to the study of low-amplitude surface deformation
- We investigate transient deformation in the eastern California shear zone

Supporting Information:

- Figures S1–S4 and Table S1

Correspondence to:

E. Tymofyeyeva,
ekmehner@ucsd.edu

Citation:

Tymofyeyeva, E., and Y. Fialko (2015), Mitigation of atmospheric phase delays in InSAR data, with application to the eastern California shear zone, *J. Geophys. Res. Solid Earth*, 120, 5952–5963, doi:10.1002/2015JB011886.

Received 9 JAN 2015

Accepted 27 JUL 2015

Accepted article online 31 JUL 2015

Published online 28 AUG 2015

Mitigation of atmospheric phase delays in InSAR data, with application to the eastern California shear zone

Ekaterina Tymofyeyeva¹ and Yuri Fialko¹

¹Institute of Geophysics and Planetary Physics, Scripps Institution of Oceanography, University of California, San Diego, La Jolla, California, USA

Abstract We present a method for estimating radar phase delays due to propagation through the troposphere and the ionosphere based on the averaging of redundant interferograms that share a common scene. Estimated atmospheric contributions can then be subtracted from the radar interferograms to improve measurements of surface deformation. Inversions using synthetic data demonstrate that this procedure can considerably reduce scatter in the time series of the line-of-sight displacements. We demonstrate the feasibility of this method by comparing the interferometric synthetic aperture radar (InSAR) time series derived from ERS-1/2 and Envisat data to continuous Global Positioning System data from eastern California. We also present results from several sites in the eastern California shear zone where anomalous deformation has been reported by previous studies, including the Blackwater fault, the Hunter Mountain fault, and the Coso geothermal plant.

1. Introduction

Recent advances in remote sensing and space-based geodetic techniques such as interferometric synthetic aperture radar (InSAR) and Global Positioning System (GPS) have led to a more detailed and accurate description of surface deformation that has benefited studies of the subsurface structure of earthquake sources [Massonnet *et al.*, 1993; Simons *et al.*, 2002; Fialko *et al.*, 2005; Johanson, 2006], the mechanical properties of seismogenic fault zones and ambient crustal rocks [Fialko *et al.*, 2002; Chen and Freymueller, 2002; Fialko, 2004a; Hamiel and Fialko, 2007], and deformation transients following significant earthquakes [Massonnet *et al.*, 1994; Jónsson *et al.*, 2003; Fialko, 2004b; Freed and Bürgmann, 2004; Barbot *et al.*, 2008]. InSAR and GPS have been also increasingly used to measure surface deformation due to active faults in the interseismic period [Peltzer *et al.*, 2001; Wright *et al.*, 2004; Fialko, 2006; Lindsey *et al.*, 2013; Kaneko *et al.*, 2013]. However, InSAR measurements of low-amplitude (subcentimeter) deformation are significantly limited by perturbations in the radar phase due to ionospheric, tropospheric, and orbital artifacts [Goldstein, 1995; Tarayre and Massonnet, 1996; Zebker *et al.*, 1997; Jehle *et al.*, 2010; Meyer, 2011]. The ionospheric phase delays are caused by the varying density of charged particles at altitudes of about 50–1000 km, while the tropospheric phase delays are dominated by variations in pressure and water content in the lowermost 10–20 km of the atmosphere [Bevis *et al.*, 1992]. The methods proposed for the reduction of the propagation artifacts include averaging of multiple independent interferograms to suppress uncorrelated noise in the radar phase [Peltzer *et al.*, 2001; Fialko and Simons, 2001; Wright *et al.*, 2004; Fialko, 2006], spatiotemporal filtering [Ferretti *et al.*, 2001; Hooper and Zebker, 2007; Schmidt and Bürgmann, 2003; Berardino *et al.*, 2002], wavelet decomposition [Hetland *et al.*, 2012], and the use of auxiliary data [Li *et al.*, 2006; Foster *et al.*, 2006; Jolivet *et al.*, 2014; Gong *et al.*, 2015]. Estimates of water vapor in the atmosphere from independent measurements have the potential to mitigate the propagation effects in studies of surface deformation, but available data typically suffer from limited coverage, cadence, and resolution. For instance, GPS estimates of atmospheric delays require dense GPS networks, and those based on meteorological models are limited in spatiotemporal resolution and accuracy [e.g., Fournier *et al.*, 2011; Wadge *et al.*, 2010; Doin *et al.*, 2009; Ding *et al.*, 2008]. The same holds for estimates of the total electron content (TEC) in the ionosphere. In this paper we present a method for the calculation of noise due to atmospheric, ionospheric, and orbital artifacts directly from the synthetic aperture radar (SAR) data. We take advantage of dense SAR catalogs to evaluate the propagation delays at every acquisition. Such catalogs will become increasingly available from the current and future InSAR missions, such as Sentinel-1, Advanced Land Observing Satellite-2, and NASA-ISRO Synthetic Aperture Radar. Our algorithm exploits the fact that

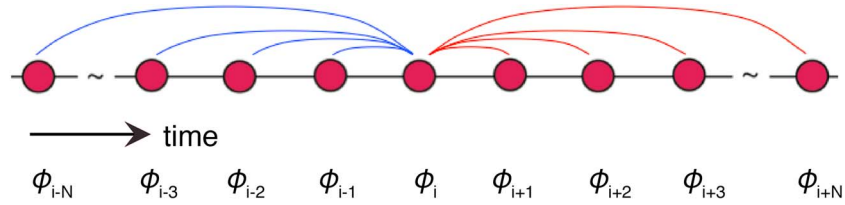


Figure 1. Averaging stencil for estimation of atmospheric phase delays. The more pairs connected to the central acquisition date, t_i , the better the estimate of the atmospheric contribution, α_i .

interferograms that share a common scene necessarily contain the same contributions from delays in the radar phase due to propagation effects.

2. Estimation of Atmospheric Phase Delays by Stacking of Dependent Interferograms

Consider two unwrapped interferograms with acquisition dates t_1 , t_2 (shared), and t_3 (see Figure S1 in the supporting information). The differential phase $\Delta\phi$ in each interferogram can be expressed as follows:

$$\Delta\phi_{12} = \Delta\tau_{12} + \alpha_2 - \alpha_1 + \epsilon_{12} \quad \Delta\phi_{23} = \Delta\tau_{23} + \alpha_3 - \alpha_2 + \epsilon_{23} \quad (1)$$

where α_i is the atmospheric contribution on the date t_i , $\Delta\tau$ is the radar phase due to surface deformation, and ϵ is the error (e.g., due to incorrect digital elevation model, antenna noise, etc). It is possible to estimate the atmospheric phase delay on the shared date, α_2 , by differencing the two interferograms, $\Delta\phi_{12} - \Delta\phi_{23}$. Note that the difference $\Delta\phi_{12} - \Delta\phi_{23}$ does not depend on surface deformation, provided that the interferograms have equal time spans and deformation occurs at a constant rate.

Combining more than two interferograms that share a common date improves the accuracy of the estimate of α , assuming that atmospheric contributions are uncorrelated in time. The accuracy of the atmospheric phase estimation for each acquisition date increases for larger aperture of the averaging stencil N (Figure 1), which guarantees an accurate recovery of the atmospheric contribution in the limit of large N :

$$\alpha_i = \lim_{N \rightarrow \infty} \frac{1}{2N} \sum_{j=1}^N \Delta\phi_{i(i-j)} - \Delta\phi_{(i+j)i} = \lim_{N \rightarrow \infty} \frac{1}{2N} \sum_{j=0}^{N-1} (N-j) [\Delta\phi_{(i-j)(i-j-1)} - \Delta\phi_{(i+j+1)(i+j)}] \quad (2)$$

The last expression in equation (2) uses interferograms from the nearest acquisition dates to minimize temporal decorrelation. This approach would be exact given a sufficiently large number of SAR acquisitions with regular intervals and good radar coherence between the nearest data takes. In practice, N is limited by the size of the data catalog and by the assumption that the deformation rate is constant over the time interval (t_{i-N}, t_{i+N}) . We therefore adopt an iterative procedure for the estimation of the atmospheric contribution, α . We begin by making an initial estimate by subtracting and averaging all the interferograms centered on each acquisition, as described above. Once an initial atmospheric phase map exists for each date, we calculate the atmospheric noise coefficient (ANC):

$$ANC_i = (10.0)(R_{\max})^{-1} \sqrt{\frac{1}{M} \sum_{m=1}^M (\alpha_i(x_m) - \bar{\alpha}_i)^2} \quad (3)$$

where $\alpha_i(x_m)$ is the atmospheric phase delay at the pixel m on the date i , and $\bar{\alpha}_i = M^{-1} \sum_{m=1}^M \alpha_i(x_m)$ is the mean value of the atmospheric phase taken over all M pixels. R_{\max} represents the RMS value of the phase screen with the highest amount of noise and is used to normalize the ANC values. The ANC quantifies the relative amount of atmospheric noise at each SAR acquisition and allows us to rank the acquisitions according to the magnitude of atmospheric contribution. In the next iteration, we recalculate α for each scene, starting with the noisiest date and using previously calculated atmospheric phase estimates to correct the interferograms used in the calculation of α for subsequent dates. The accuracy of the atmospheric phase estimates decreases toward the ends of the catalog, where shorter and/or one-sided averaging stencils need to be used.

If the time spans of the interferograms used in the averaging procedure are not equal, or the deformation signal is not linear in time, atmospheric phase maps α_i computed using equation (1) may contain a nonnegligible contribution from the deformation signal, $\Delta\tau$. In case of slowly varying (compared to the satellite revisit time, Δt) deformation, we adopt the following procedure for separate estimation of $\Delta\tau$ and α_i .

First, we generate time series of range changes [e.g., *Schmidt and Bürgmann, 2003*] at each of the pixels that remain coherent in all interferograms, with respect to a reference pixel assumed to have zero velocity. We estimate the tectonic signal by fitting a smoothing spline [*De Boor, 1978*] to the time series. The inferred time-dependent surface deformation, $\Delta\tau$, is then subtracted from interferograms prior to the calculation of atmospheric phase delays.

This process, repeated iteratively until convergence, improves the separate estimates of time-dependent deformation and the atmospheric contributions for each acquisition date. We then subtract the obtained atmospheric phase maps from the original interferograms and compute time series and maps of mean line-of-sight (LOS) velocities from the corrected data.

3. Validation With Synthetic Data

We validated our method by inverting synthetic data that contain realistic atmospheric noise and a known deformation signal. The synthetic data set was created using the atmospheric phase maps calculated for ERS and Envisat track 170 in Southern California at each acquisition date (Figure S2). Synthetic interferograms were made by differencing the atmospheric phase on the respective dates and adding a time-dependent low-amplitude deformation signal. Results of the synthetic test are shown in Figure 2. In the first test, we assumed regular SAR acquisitions and baselines small enough to make it possible to form interferograms between any two scenes. This is an ideal scenario for radar interferometry that may soon be realized thanks to better control of satellite orbits and more frequent and regular acquisitions of recently launched as well as planned InSAR missions. The algorithm recovers both secular trends and nonlinear signals of amplitudes as small as 1 mm/yr in the radar line of sight. As one can see from Figure 2a, there is an improvement in accuracy of the recovered signal in the time series corrected for the propagation effects, compared to the standard least squares solution, which makes it possible to resolve low-amplitude signals that would otherwise be hidden in the noise.

In order to quantify the accuracy of the method, we compared the atmospheric phase maps retrieved using our algorithm from the synthetic data set to the ones originally used to create the synthetic interferograms. We have found that the method recovers up to 95% of the atmospheric noise in the synthetic data and over 70% of the atmospheric signal in more than 50% of the cases. We also investigated the effect of irregular data acquisitions and baselines by creating a synthetic data set in the same way as described above but using baselines and acquisition dates from the actual ERS and Envisat catalogs (Figure 3). Even though the amount of scatter in the corrected time series is greater due to a large spread in baselines and uneven time spans (Figure 2b), the method retrieves deformation signals of similar amplitudes as in the ideal case. Comparing retrieved atmospheric phase maps to those used to create synthetic data, we found that we were able to recover up to 85% of the atmospheric signal, with more than 50% of the signal recovered for more than half of the synthetic phase maps. Because of limited network connectivity, for some of the pairs the method retrieved less than 10% of the atmospheric contribution. Examples of successful and unsuccessful estimation of synthetic atmospheric phase maps are presented in the supporting information Figure S3.

Note that the input signals in our tests are very well sampled by the data. The recovery of short-period deformation signals depends on the frequency of data acquisitions by the SAR satellite, as well as the length of the averaging stencil, N , used to compute the atmospheric phase maps. In our validation experiment, we have used stencils varying between 0 and 2 years for data sets with irregular acquisitions and less than 1 year for well-connected, regularly spaced data acquired every 30 days.

In addition to time series, we also calculated an average line-of-sight velocity map (see Figure 4). The average velocities were obtained by computing time series of cumulative displacements at every pixel, fitting a smoothing spline as described above, subtracting the spline values at the beginning and end of the time interval of interest, t_1 and t_N , and dividing by the time span ($t_1 - t_N$). We compare our result to LOS velocities calculated using conventional stacking of the 257 interferograms in the synthetic catalog, without the atmospheric correction. Figure 4 shows a reduction in the atmospheric noise when the correction is applied, as compared to the uncorrected version of the stack.

In principle, the limitation of the interferometric connectivity of the data catalog can be mitigated using a small-baseline subset (SBAS)-like approach [e.g., *Pepe et al., 2011; Fattahi and Amelung, 2013*]. Upon computing time series of displacements for each coherent pixel on each date, one can form additional interferograms

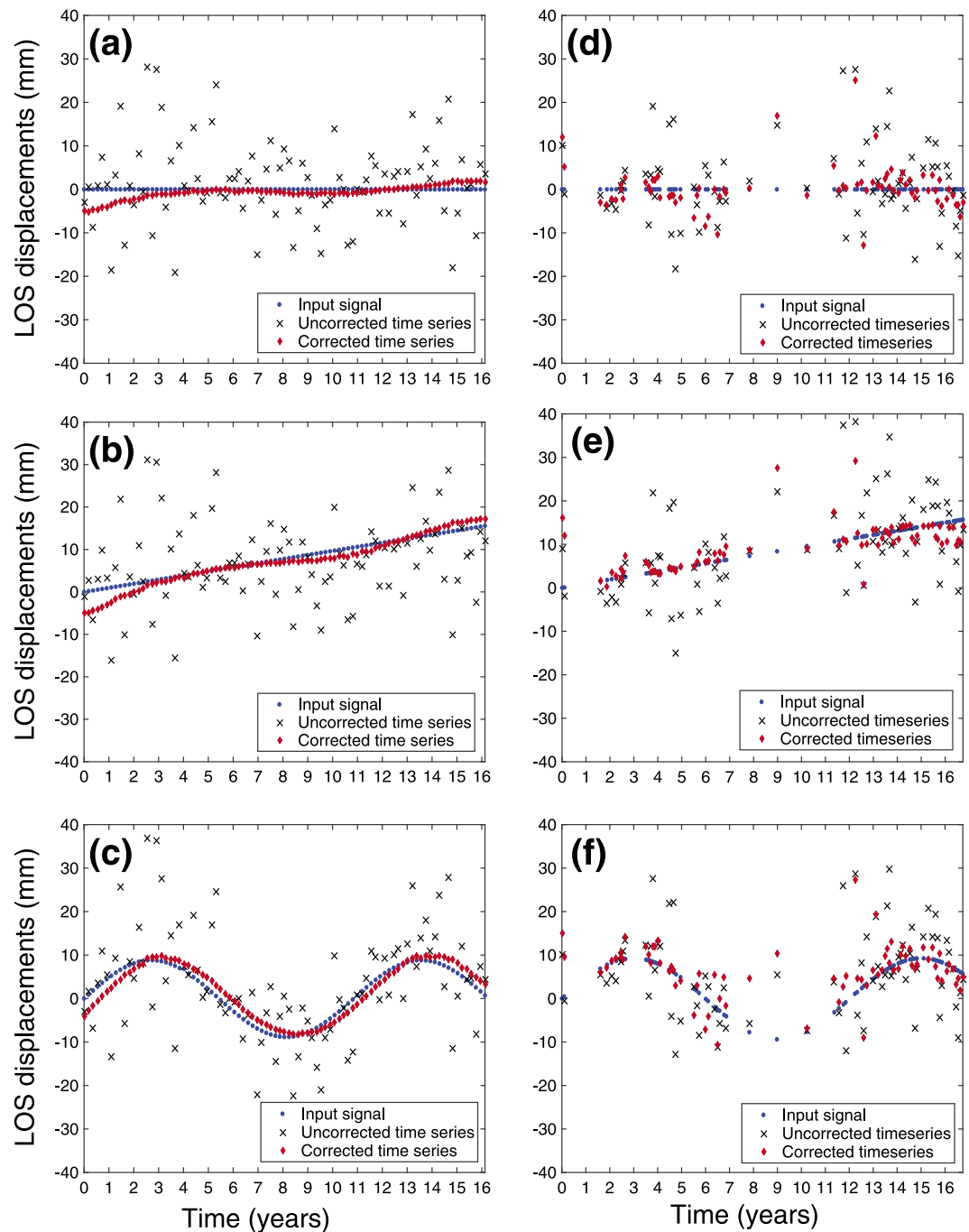


Figure 2. Results of the synthetic data test. (a–c) Regular acquisitions with small baselines. (d–f) Set of interferograms that mimic the ERS/Envisat baseline distribution (Figure 3). No deformation (Figures 2a and 2d). Constant velocity of 1 mm/yr (Figures 2b and 2e). Variable velocity (Figures 2c and 2f). Blue dots denote prescribed deformation signal, and red dots and crosses denote recovered time series with and without atmospheric corrections, respectively.

by subtracting the phase between any two dates. These new interferograms can then be used alongside preexisting interferograms to estimate the atmospheric contribution for each scene.

4. Comparison to Continuous GPS Time Series

In addition to the tests using synthetic data, we validated our method by performing a comparison of the InSAR time series to those recorded by continuous GPS stations. GPS measurements have the

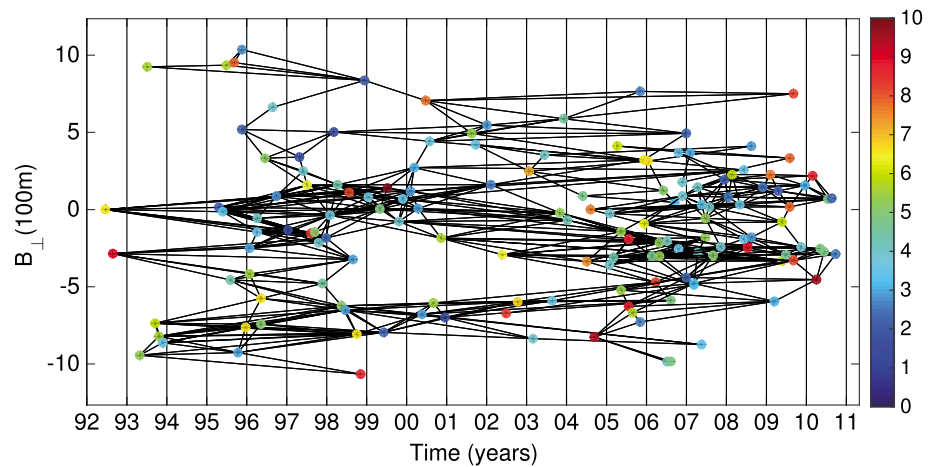


Figure 3. Baseline plot for ERS/Envisat track 170. The colored dots indicate the acquisition dates, and the lines indicate interferograms used in our analysis. The colors of the dots denote the value of the atmospheric noise coefficient (ANC) calculated using equation (3). The cold colors correspond to low values of the ANC, and the warm colors correspond to high values of ANC.

advantage of a much higher temporal sampling rate and better resolving phase delays due to atmospheric and ionospheric variability.

The raw SAR data were processed using the JPL/Caltech software ROI_PAC. The topography correction was applied using the digital elevation model from the Shuttle Radar Topography Mission. The interferograms were not flattened to remove possible orbital errors, as this could violate assumptions behind equation (2). We also did not correct for the Envisat clock drift. The InSAR time series were calculated using the procedure described by Schmidt and Bürgmann [2003].

Figure 3 shows an example of Atmospheric Noise Coefficients calculated using our method for SAR data from the ERS-1/2 and Envisat track 170 (Mojave Desert, eastern California). The calculated range changes due to propagation effects (atmospheric phase maps) are shown in Figure S2 and Table S1 of the supporting information. We are able to combine the ERS and Envisat data into a single data set because there are several interferograms that were acquired on the same dates by ERS-2 and Envisat, separated by 30 min. These interferograms have essentially identical contributions from atmospheric phase delays (see Figure S4 of the supporting information).

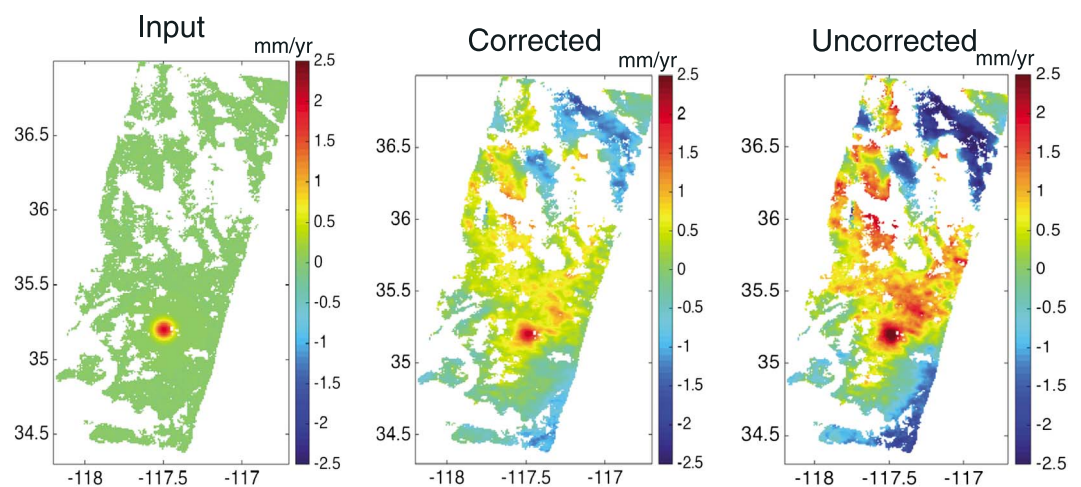


Figure 4. A mean line-of-sight velocity map retrieved by the proposed atmospheric correction method, using synthetic data from a set of interferograms that mimic the ERS/Envisat data catalog. (left) The original input LOS velocities, with no atmospheric noise. (middle) The mean velocities retrieved using atmospheric correction. (right) Velocities obtained using conventional stacking of the synthetic interferograms.

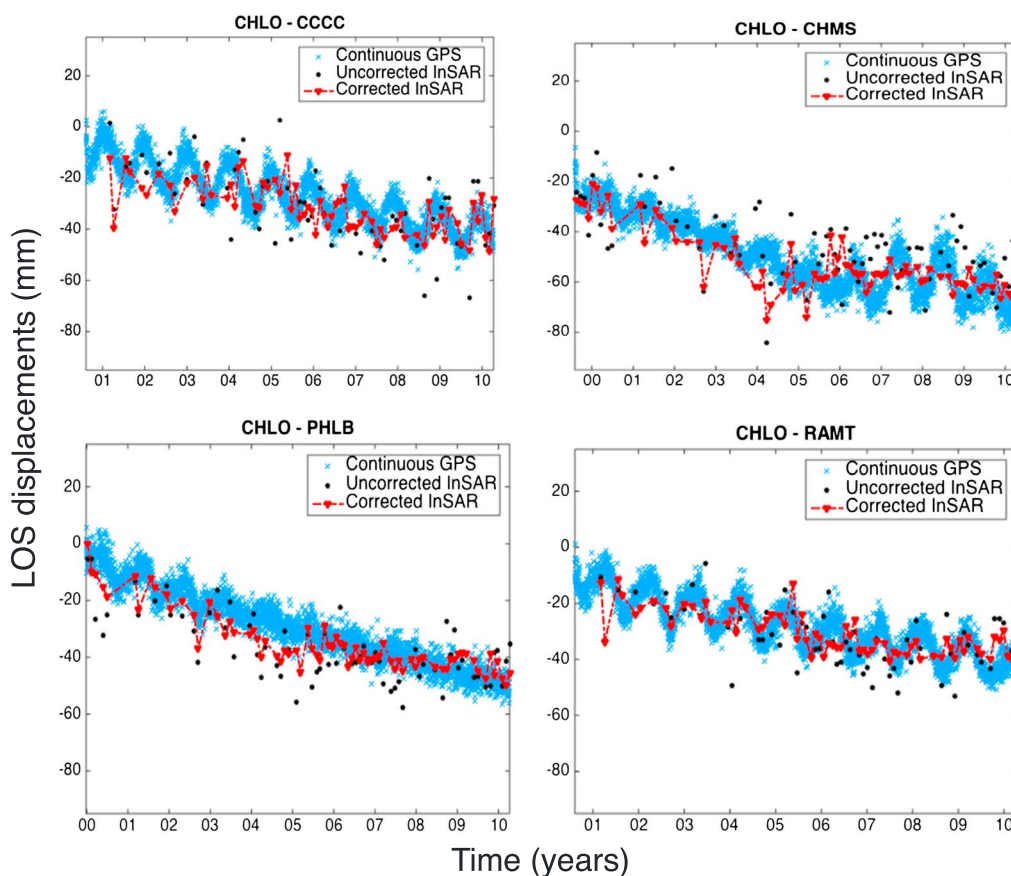


Figure 5. Comparison of InSAR time series with continuous GPS. The large distance between the chosen GPS sites implies that the atmospheric noise is not correlated between the stations.

There are few continuous GPS stations that have been in operation long enough to provide an instructive comparison to the InSAR data, which span the time period between 1992 and 2010. We selected five stations that began collecting data in the year 2000 and calculated time series between the reference station, CHLO, and each of the remaining four stations. The three-component (east, north, and vertical) GPS displacements were projected onto the InSAR line of sight using local incidence angles. The InSAR time series (Figure 5) show good agreement with the GPS measurements, as well as a reduction in scatter when we correct for the propagation delays. In some cases, the corrected InSAR time series were able to recover the seasonal signals visible in the GPS, indicating differential motion with respect to the reference site. In other cases, the periodic signal present in the GPS is muted in the InSAR time series, possibly due to long-wavelength seasonal variations in the water content in the troposphere or due to local effects (e.g., a tree planted near site CHMS introduced a spurious displacement signal due to seasonal growth cycles after year 2006).

5. Application to the Eastern California Shear Zone

We apply the method described in section 2 to study secular and transient crustal deformation in the eastern California shear zone. The eastern California shear zone (ECSZ) is a complex seismically active network of Quaternary faults that accommodates between 10 and 20% of the relative motion between the Pacific and North American plates [Sauber *et al.*, 1986; Dokka and Travis, 1990]. It has been proposed that the ECSZ represents an incipient plate boundary forming in response to changes in the orientation of the regional tectonic stress [Nur *et al.*, 1993]. Space geodetic observations have documented a wide range of processes affecting surface displacements in the ECSZ, including coseismic [e.g., Simons *et al.*, 2002; Fialko *et al.*, 2002; Fialko, 2004a], postseismic [Peltzer *et al.*, 1998; Fialko, 2004b], and interseismic [Peltzer *et al.*, 2001; Gourmelen *et al.*, 2011] deformation and ground subsidence [e.g., Fialko and Simons, 2000; Solt and Sneed, 2014]. Figure 6 shows the average LOS velocities from three satellite tracks over the eastern California shear zone. The average LOS velocities were conformed to the regional GPS velocity field using the SURF algorithm [Tong *et al.*, 2013].

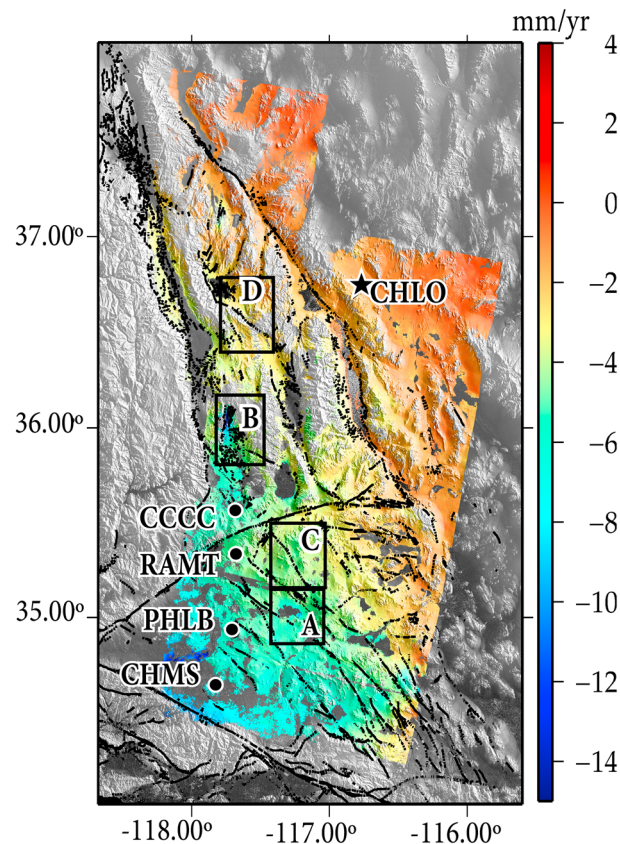


Figure 6. Average line-of-sight velocity from ERS and Envisat tracks 170, 399, and 442, computed using atmospheric corrections. The locations of the GPS stations used for comparison with InSAR time series are marked by black circles, and the reference station is marked by a black star. The outlined areas A, B, C, and D correspond to our focus areas in the eastern California shear zone: Harper Lake, Coso subsidence, Blackwater fault, and Hunter Mountain fault, respectively. Positive LOS velocity indicates motion toward the satellite.

Figure 7a shows the mean line-of-sight velocities over the years 1992–2010, from overlapping ERS/Envisat tracks 170 and 399. The central area of the lakebed is decorrelated, but the InSAR data clearly show subsidence around the edge of Harper Lake, consistent with the results of the previous study [Solt and Sneed, 2014]. Figures 7b and 7c show the average line-of-sight velocities from a 5 km wide north-south profile across the lake (endpoints indicated by the stars in Figure 7a). The data show increases in the radar range of about 4 mm/yr along the north shore of Harper Lake. Figure 7b shows the average LOS velocities obtained using conventional stacking of radar interferograms, while Figure 7c shows the average LOS velocities calculated using atmospheric corrections. As one can see in Figure 7b, there is a systematic difference of about 1 mm/yr in the LOS velocities from tracks 170 and 399 at the southern end of the profile. This difference disappears in the LOS velocities corrected for atmospheric artifacts using the method described in section 2 (Figure 7c). A better agreement between data from the two independent data sets from tracks 170 and 399 provides further validation for the robustness of the algorithm. A small mismatch in the LOS velocities from the two overlapping tracks starting at the approximate longitude -117.2 and continuing to the northeast may be due to residual atmospheric effects or differences in the local incidence angles.

5.2. Subsidence at the Coso Geothermal Plant

The Coso geothermal field lies in the transition zone between the San Andreas Fault and the Basin and Range province [Walter and Weaver, 1980; Roquemore, 1980]. Its primary heat source is believed to be related to a large magmatic system [Duffield et al., 1980]. This geothermal resource is exploited by the Coso geothermal plant, the second largest geothermal plant in the United States. The area is tectonically active with a great deal

Here we consider several areas where anomalous deformation signals were identified by previous studies. We start by examining the subsidence around Harper Lake [Solt and Sneed, 2014], where we take advantage of the data from two overlapping InSAR tracks to assess the robustness of the method. We then examine ground subsidence around the Coso geothermal plant [Fialko and Simons, 2000] and show that the subsidence has continued at a constant rate throughout the 20 year time period spanned by the InSAR data catalog. Finally, we investigate deformation across the Blackwater and Hunter Mountain faults, where previous studies have suggested anomalously large slip rates and shallow locking depths [Peltzer et al., 2001; Gourmelen et al., 2011].

5.1. Subsidence at Harper Lake

Harper Lake is located south of the Blackwater-Calico fault system, in the middle of an area of active deformation in the eastern California shear zone. Various geologic and geodetic observations indicate that the entire lakebed is consistently subsiding. For example, Solt and Sneed [2014] investigated the extent and mechanisms of subsidence around Harper Lake, as well as those of several other lakebeds in the Mojave Desert, using InSAR data from the years 2005–2009. They suggested that the deformation was likely due to the compaction of fine-grained paleo-lakebed deposits in response to changing groundwater levels.

Figure 7a shows the mean line-of-sight velocities over the years 1992–2010, from overlapping

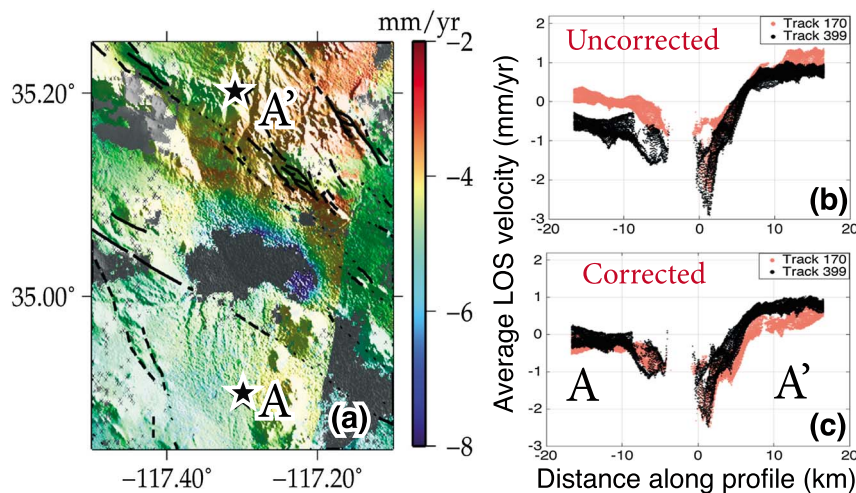


Figure 7. (a) Average line-of-sight (LOS) velocities from ERS/Envisat tracks 170 and 399, in the vicinity of Harper Lake. (b) Profile AA' across Harper Lake. Red dots show average LOS velocity from track 170, and black dots show average LOS velocity from track 399. (c) Same as Figure 7b but with the average LOS velocities computed using corrections for the propagation delays.

of seismicity that can be attributed to both natural and man-made processes [Feng and Lees, 1998; Fialko and Simons, 2000]. InSAR and GPS studies have shown that this seismicity can be linked to the subsidence of the Coso geothermal field. Possible causes of the subsidence include net fluid withdrawal, thermal contraction and depletion of the reservoir, and compaction of the host rocks because of a decrease in pore pressure.

Fialko and Simons [2000] used eight interferometric pairs from the time period between the years 1993 and 1999 to investigate the deformation around the Coso geothermal plant and understand the causes and mechanisms that govern the subsidence in the area. The study found a spatially complex deformation pattern characterized by two localized subsidence peaks, and a line-of-sight velocity signal of 3–4 cm/yr at the center of the anomaly. By analyzing consecutive interferograms, Fialko and Simons [2000] showed that the subsidence peaks become broader with time, suggesting that the deformation at Coso may be time dependent.

Figure 8a shows the average LOS velocities from the Coso area obtained from our analysis of the ERS-1/2 and Envisat data spanning 1992–2010. The time series of deformation reveal that the subsidence has occurred at an essentially constant rate over the past 20 years (Figure 8b). The point near the center of the subsidence marked by a star in Figure 8b has been subsiding at a rate of about 20 mm/yr. The deformation signal here is large enough that the atmospheric corrections make a relatively small difference, although one can still see a reduction in scatter between the corrected and the uncorrected time series.

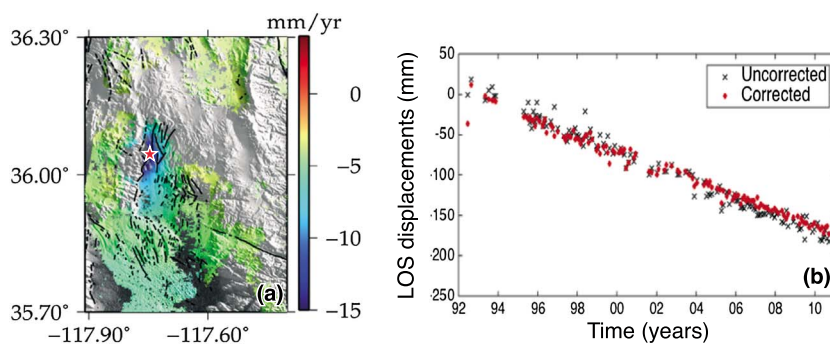


Figure 8. (a) LOS velocity map of the area around the Coso geothermal plant. The star marks a location for which the time series were computed with respect to a distant (approximately 70 km away to the NE) reference point. (b) Time history of surface displacement along the satellite line of sight at a point marked by the star in Figure 8a.

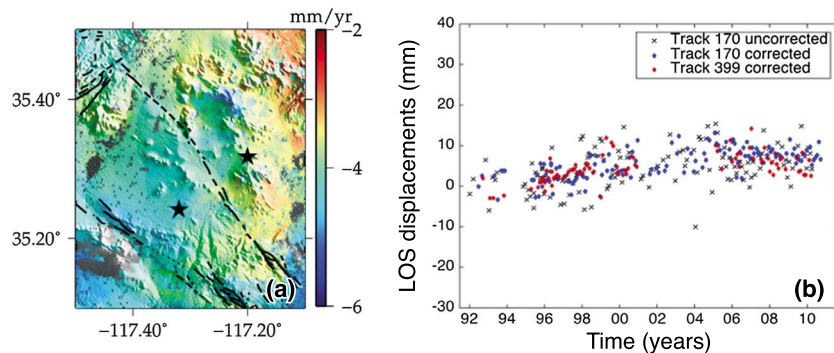


Figure 9. (a) Average LOS velocities around the Blackwater fault from our analysis of ERS-1/2 and Envisat tracks 170 and 399. (b) Time series of displacements calculated between two points across the fault (denoted by black stars). Time series show an elevated velocity between 1992 and 2000, consistent with findings of *Peltzer et al.* [2001], but a slowdown (or possibly a reversal) after 2000.

5.3. Deformation Across the Blackwater Fault

The Calico-Blackwater fault system is the longest in the Mojave Desert, trending northeast, and is intersected by the Garlock fault to the north. It has been proposed that the Calico-Blackwater fault system accommodates a large portion of the right-lateral slip in the eastern California shear zone, but there is a general disagreement between geologic and geodetic slip rate estimates. Geologic studies estimate the slip rate of 1–2 mm/yr on the Blackwater fault [*Dokka and Travis, 1990*]. *Peltzer et al.* [2001] reported a much higher slip rate of about 7 mm/yr based on the analysis of ERS-1/2 data from track 170 spanning the years 1992–2000. They attributed the high slip rate to transient deformation following the 1992 Landers earthquake. *Peltzer et al.* [2001] also inferred an anomalously shallow locking depth of 5 km. To investigate the nature of the anomalous deformation on the Blackwater fault, we have analyzed all available InSAR data from ERS-1/2 and Envisat tracks 170 and 399, spanning a time period between 1992 and 2010. Figure 9a shows an overlay of the average LOS velocities from the two satellite tracks (data from track 399 at the bottom, data from track 170 on top) from an area of overlap around the Blackwater fault. The data do not show a sharp LOS velocity gradient across the fault trace. To get an insight into possible time-dependent deformation processes within the fault zone, we calculated time series of LOS displacements between points on two sides of the fault, as indicated by the stars in Figure 9a. The results are shown in Figure 9b.

The time series from the two tracks, corrected for propagation artifacts (colored symbols in Figure 9b), are in good agreement with each other and are considerably less scattered compared to the “uncorrected” time series (crosses in Figure 9b). The data from both tracks show a systematic velocity trend of about 1.5 mm/yr between the years 1992 and 2000, which is consistent with the result from *Peltzer et al.* [2001], who inferred a mean LOS velocity across the fault of approximately the same magnitude over the same time period. After the year 2000, our results indicate a decrease, or perhaps even a reversal, in the LOS velocities between different sides of the fault. Thus, the anomalously high strain rates due to the Blackwater fault reported by *Peltzer et al.* [2001] are not representative of secular deformation and could possibly reflect postseismic transient due to the 1992 Landers earthquake.

We also point out that it is not clear whether the elevated LOS velocities across the fault over the 1992–2000 period were due to horizontal fault-parallel displacements. Alternatively, they could be caused by differential vertical motion of the east side of the fault with respect to its west side, at rates that are much smaller than the deduced horizontal rates but comparable to the observed LOS velocities of the order of 1 mm/yr. Unfortunately, very little data from the ascending ERS-1/2 orbits exist for the study area, making it difficult to test this hypothesis.

5.4. Deformation Across the Hunter Mountain Fault

The Hunter Mountain fault is located north of the Garlock fault, at the eastern boundary of the Sierra Nevada range. It connects with the faults of Saline Valley to the northwest and Panamint Valley to the southeast [*Burchfiel et al., 1987*]. The Hunter Mountain fault is a relatively young feature that has formed between approximately 2.8 Ma and 4.0 Ma [*Burchfiel et al., 1987; Hodges et al., 1989; Lee et al., 2009*].

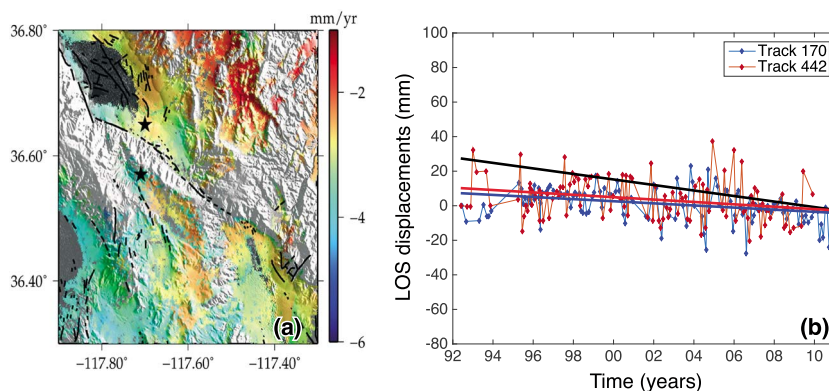


Figure 10. (a) Average LOS velocities from an area around the Hunter Mountain fault. (b) Time series between two points (black stars, approximately 8 km apart) across the Hunter Mountain fault over the time period between 1992 and 2010. Thick blue and red lines denote the least squares fits to the time series from tracks 170 and 442, respectively. Thick black line denotes the average LOS velocity across the fault reported by *Gourmelen et al.* [2011].

Gourmelen et al. [2011] investigated the deformation due to the Hunter Mountain fault by analyzing 44 interferograms from satellite track 442 of the satellites ERS-1/2, from the time period between the years 1992 and 2000. They processed the data using the SBAS method, which evaluates atmospheric effects using a spatiotemporal filter [*Ferretti et al.*, 2001; *Berardino et al.*, 2002]. Average line-of-sight velocities derived from the InSAR data revealed deformation at a rate of 1.6 mm/yr in a localized zone several kilometers wide, centered on the fault. Interpreting the data in terms of the buried dislocation model [*Savage and Burford*, 1973] resulted in a slip rate of approximately 5 mm/yr, above the geologic slip rate of 3.3 mm/yr [*Lee et al.*, 2009], and an anomalously shallow locking depth of about 2 km. *Gourmelen et al.* [2011] proposed that the discrepancy between geologic and geodetic slip rates may be due to the fact that the relatively young Hunter Mountain fault may be undergoing evolution and acceleration.

We have combined InSAR data from the ERS-1/2 and Envisat satellites from overlapping tracks 442 and 170 over the years 1992 to 2010 to compute average LOS velocities as well as time series of LOS displacements across the Hunter Mountain fault. The data in Figure 10a show a much smaller velocity gradient across the fault than observed by *Gourmelen et al.* [2011].

To check for a possible temporally varying signal, we computed line-of-sight displacement time series between two points where the variation in average LOS velocities on the different sides of the fault seems to be at its highest and where track 442 overlaps with ERS/Envisat track 170. The time series exhibit a significant amount of scatter, possibly due to seasonal variability in atmospheric delays (correlated with topography) or seasonal cycles of uplift and subsidence (Figure 10b). The best fitting linear trends to the time series from both tracks (thick red and blue lines in Figure 10b) indicate LOS velocities of less than a millimeter per year, substantially smaller than the velocity inferred by *Gourmelen et al.* [2011] (black line in Figure 10b) and likely within the measurement uncertainty. Therefore, we conclude that neither the anomalously high slip rate nor the shallow locking depth on the Hunter Mountain fault are required by the data.

6. Conclusions

We have developed a method to mitigate the noise due to propagation effects in InSAR data, such as those caused by tropospheric and ionospheric phase delays. The method takes advantage of the fact that the interferograms that share a common date also share the same propagation delay due to the atmosphere or long-wavelength “ramp” due to imprecise knowledge of spacecraft orbits. Because the method relies on spatial patterns to identify propagation artifacts, it works best in areas of good radar coherence. It also relies on large data sets with good interferometric connectivity between radar acquisitions, such as the example shown in Figure 3. It allows one to measure deformation signals that are slowly varying compared to the interval between radar acquisitions (Figure 2).

Tests using synthetic data are able to recover up to 95% of the atmospheric signal. We have also tested the robustness of our method by comparing the average line-of-sight velocities from different satellite tracks

covering the same area and with continuous GPS data. The results show good agreement and accuracy of about a millimeter per year in the satellite line of sight.

We applied our method to several areas in the eastern California shear zone where anomalous deformation has been reported by previous studies [Peltzer *et al.*, 2001; Gourmelen *et al.*, 2011; Fialko and Simons, 2000]. Subsidence associated with the Coso geothermal field persisted at a constant rate of a few centimeters per year over the time period between the years 1992 and 2010. The deformation across the Blackwater fault occurred at a nearly constant rate of 1.5 mm/yr in the satellite LOS between 1992 and 2000, consistent with the study by Peltzer *et al.* [2001], but stopped, or perhaps even reversed, in 2000–2010. We do not observe a resolvable deformation signal across the Hunter Mountain fault, where a study by Gourmelen *et al.* [2011] suggested higher than geologic slip rates and an anomalously shallow locking depth of 2 km. We speculate that the mean LOS velocity estimates by Gourmelen *et al.* [2011] might be biased by large seasonal variations in the LOS velocities at small (few kilometers) spatial scales around the fault.

The method presented here can be used to estimate atmospheric propagation delays as well as orbital errors, provided that they are uncorrelated in time, without relying on auxiliary data. The correction improves the accuracy of InSAR measurements of low-amplitude quasi-steady deformation of the Earth's surface.

Acknowledgments

This work was supported by NASA grant NNX14AQ15G and the Southern California Earthquake Center. Data are available from the authors. Codes can be downloaded at <http://igppweb.ucsd.edu/~ekmehner/projects.html>. We thank the Associate Editor and two anonymous reviewers for comments that improved this manuscript. We also thank Diane Rivet, who contributed to the development of the computer codes used in this study.

References

- Barbot, S., Y. Fialko, and D. Sandwell (2008), Effect of a compliant fault zone on the inferred earthquake slip distribution, *J. Geophys. Res.*, *113*, B06404, doi:10.1029/2007JB005256.
- Berardino, P., G. Fornaro, R. Lanari, and E. Sansosti (2002), A new algorithm for surface deformation monitoring based on small baseline differential SAR interferograms, *IEEE Trans. Geosci. Remote Sens.*, *40*(11), 2375–2383, doi:10.1109/TGRS.2002.803792.
- Bevis, M., S. Businger, T. A. Herring, C. Rocken, R. A. Anthes, and R. H. Ware (1992), GPS meteorology: Remote sensing of atmospheric water vapor using the Global Positioning System, *J. Geophys. Res.*, *97*(D14), 15,787–15,801, doi:10.1029/92JD01517.
- Burchfiel, B. C., K. V. Hodges, and L. H. Royden (1987), Geology of Panamint Valley-Saline Valley Pull-Apart System, California: Palinspastic evidence for low-angle geometry of a Neogene Range-Bounding fault, *J. Geophys. Res.*, *92*(B10), 10,427–10,426, doi:10.1029/JB092iB10p10422.
- Chen, Q., and J. Freymueller (2002), Geodetic evidence for a near-fault compliant zone along the San Andreas Fault in the San Francisco Bay area, *Bull. Seismol. Soc. Am.*, *92*(2), 656–671, doi:10.1785/0120010110.
- De Boor, C. (1978), *A Practical Guide to Splines*, Springer, New York.
- Ding, X., Z. Li, J. Zhu, G. Feng, and J. Long (2008), Atmospheric effects on InSAR measurements and their mitigation, *Sensors*, *8*(9), 5426–5448, doi:10.3390/s8095426.
- Doin, M. P., C. Lasserre, G. Peltzer, O. Cavalié, and C. Doubre (2009), Corrections of stratified tropospheric delays in SAR interferometry: Validation with global atmospheric models, *J. Appl. Geophys.*, *69*(1), 35–50, doi:10.1016/j.jappgeo.2009.03.010.
- Dokka, R., and C. Travis (1990), Late Cenozoic strike-slip faulting in the Mojave Desert, California, *Tectonics*, *9*(2), 311–340, doi:10.1029/TC009i002p00311.
- Duffield, W. A., C. R. Bacon, and G. B. Dalrymple (1980), Late Cenozoic volcanism, geochronology, and structure of the Coso Range, Inyo County, California, *J. Geophys. Res.*, *85*(B5), 2381–2404, doi:10.1029/JB085iB05p02381.
- Fattahi, H., and F. Amelung (2013), DEM error correction in InSAR time series, *IEEE Trans. Geosci. Remote Sens.*, *51*(7), 4249–4259, doi:10.1109/TGRS.2012.2227761.
- Feng, Q., and J. M. Lees (1998), Microseismicity, stress, and fracture in the Coso geothermal field, California, *Tectonophysics*, *289*(1–3), 221–238, doi:10.1016/S0040-1951(97)00317-X.
- Ferretti, A., C. Prati, and F. Rocca (2001), Permanent scatterers in SAR interferometry, *IEEE Trans. Geosci. Remote Sens.*, *39*(1), 8–20, doi:10.1109/36.898661.
- Fialko, Y. (2004a), Probing the mechanical properties of seismically active crust with space geodesy: Study of the coseismic deformation due to the 1992 M_w 7.3 Landers (Southern California) earthquake, *J. Geophys. Res.*, *109*, B03307, doi:10.1029/2003JB002756.
- Fialko, Y. (2004b), Evidence of fluid-filled upper crust from observations of postseismic deformation due to the 1992 M_w 7.3 Landers earthquake, *J. Geophys. Res.*, *109*, B08401, doi:10.1029/2004JB002985.
- Fialko, Y. (2006), Interseismic strain accumulation and the earthquake potential on the southern San Andreas Fault system, *Nature*, *441*(7096), 968–971, doi:10.1038/nature04797.
- Fialko, Y., and M. Simons (2000), Deformation and seismicity in the Coso geothermal area, Inyo County, California: Observations and modeling using satellite radar interferometry, *J. Geophys. Res.*, *105*(B9), 21,781–21,793, doi:10.1029/2000JB900169.
- Fialko, Y., and M. Simons (2001), Evidence for on-going inflation of the Socorro Magma Body, New Mexico, from interferometric synthetic aperture radar imaging, *Geophys. Res. Lett.*, *28*(18), 3549–3552, doi:10.1029/2001GL013318.
- Fialko, Y., D. Sandwell, D. Agnew, M. Simons, and B. Minster (2002), Deformation on nearby faults induced by the 1999 Hector Mine earthquake, *Science*, *297*(5588), 1858–62, doi:10.1126/science.1074671.
- Fialko, Y., D. Sandwell, M. Simons, and P. Rosen (2005), Three-dimensional deformation caused by the Bam, Iran, earthquake and the origin of shallow slip deficit, *Nature*, *435*(7040), 295–299, doi:10.1038/nature03425.
- Foster, J., B. Brooks, T. Cherubini, C. Shacat, S. Businger, and C. L. Werner (2006), Mitigating atmospheric noise for InSAR using a high resolution weather model, *Geophys. Res. Lett.*, *33*, L16304, doi:10.1029/2006GL026781.
- Fournier, T., M. E. Pritchard, and N. Finnegan (2011), Accounting for atmospheric delays in InSAR data in a search for long-wavelength deformation in South America, *IEEE Trans. Geosci. Remote Sens.*, *49*(10), 3856–3867, doi:10.1109/TGRS.2011.2139217.
- Freed, A. M., and R. Bürgmann (2004), Evidence of power-law flow in the Mojave Desert mantle, *Nature*, *430*(6999), 548–551, doi:10.1038/nature02784.
- Goldstein, R. (1995), Atmospheric limitations to repeat-track radar interferometry, *Geophys. Res. Lett.*, *22*(18), 2517–2520, doi:10.1029/95GL02475.

- Gong, W., F. J. Meyer, S. Liu, and R. F. Hanssen (2015), Temporal filtering of InSAR data using statistical parameters from NWP models, *IEEE Trans. Geosci. Remote Sens.*, *53*(7), 4033–4044, doi:10.1109/TGRS.2015.2389143.
- Gourmelen, N., T. H. Dixon, F. Amelung, and G. Schmalzle (2011), Acceleration and evolution of faults: An example from the Hunter Mountain Panamint Valley fault zone, eastern California, *Earth Planet. Sci. Lett.*, *301*(1–2), 337–344, doi:10.1016/j.epsl.2010.11.016.
- Hamiel, Y., and Y. Fialko (2007), Structure and mechanical properties of faults in the North Anatolian Fault system from InSAR observations of coseismic deformation due to the 1999 Izmit (Turkey) earthquake, *J. Geophys. Res.*, *112*, B07412, doi:10.1029/2006JB004777.
- Hetland, E. A., P. Musé, M. Simons, Y. N. Lin, P. S. Agram, and C. J. DiCaprio (2012), Multi-scale InSAR Time Series (MInTS) analysis of surface deformation, *J. Geophys. Res.*, *117*, B02404, doi:10.1029/2011JB008731.
- Hodges, K., L. McKenna, J. Stock, and J. Knapp (1989), Evolution of extensional basins and basin and range topography west of Death Valley, California, *Tectonics*, *8*(3), 453–467, doi:10.1029/TC008i03p00453.
- Hooper, A., and H. A. Zebker (2007), Phase unwrapping in three dimensions with application to InSAR time series, *J. Opt. Soc. Am. A Opt. Image Sci.*, *24*(9), 2737–2747, doi:10.1364/JOSAA.24.002737.
- Jehle, M., O. Frey, D. Small, and E. Meier (2010), Measurement of ionospheric TEC in spaceborne SAR data, *IEEE Trans. Geosci. Remote Sens.*, *48*(6), 2460–2468, doi:10.1109/TGRS.2010.2040621.
- Johanson, I. A. (2006), Coseismic and postseismic slip of the 2004 Parkfield earthquake from space-geodetic data, *Bull. Seismol. Soc. Am.*, *96*(4B), S269–S282, doi:10.1785/0120050818.
- Jolivet, R., P. S. Agram, N. Y. Lin, M. Simons, M. P. Doin, G. Peltzer, and Z. Li (2014), Improving InSAR geodesy using global atmospheric models, *J. Geophys. Res. Solid Earth*, *119*, 2324–2341, doi:10.1002/2013JB010588.
- Jónsson, S., P. Segall, R. Pedersen, and G. Björnsson (2003), Post-earthquake ground movements correlated to pore-pressure transients, *Nature*, *424*(6945), 179–183, doi:10.1038/nature01776.
- Kaneko, Y., Y. Fialko, D. T. Sandwell, X. Tong, and M. Furuya (2013), Interseismic deformation and creep along the central section of the North Anatolian Fault (Turkey): InSAR observations and implications for rate-and-state friction properties, *J. Geophys. Res. Solid Earth*, *118*(1), 316–331, doi:10.1029/2012JB009661.
- Lee, J., D. F. Stockli, L. A. Owen, R. C. Finkel, and R. Kisilitsyn (2009), Exhumation of the Inyo Mountains, California: Implications for the timing of extension along the western boundary of the Basin and Range Province and distribution of dextral fault slip rates across the eastern California shear zone, *Tectonics*, *28*, TC1001, doi:10.1029/2008TC002295.
- Li, Z., X. Ding, C. Huang, G. Wadge, and D. Zheng (2006), Modeling of atmospheric effects on InSAR measurements by incorporating terrain elevation information, *J. Atmos. Sol. Terr. Phys.*, *68*(11), 1189–1194, doi:10.1016/j.jastp.2006.03.002.
- Lindsey, E. O., V. J. Sahakian, Y. Fialko, Y. Bock, S. Barbot, and T. K. Rockwell (2013), Interseismic strain localization in the San Jacinto Fault Zone, *Pure Appl. Geophys.*, *171*(11), 2937–2954, doi:10.1007/s00024-013-0753-z.
- Massonnet, D., M. Rossi, C. Carmona, F. Adragna, G. Peltzer, K. Feigl, and T. Rabaute (1993), The displacement field of the Landers earthquake mapped by radar interferometry, *Nature*, *364*(6433), 138–142, doi:10.1038/364138a0.
- Massonnet, D., K. Feigl, M. Rossi, and F. Adragna (1994), Radar interferometric mapping of deformation in the year after the Landers earthquake, *Nature*, *369*, 227–230, doi:10.1038/369227a0.
- Meyer, F. J. (2011), Performance requirements for ionospheric correction of low-frequency SAR data, *IEEE Trans. Geosci. Remote Sens.*, *49*(10), 3694–3702, doi:10.1109/TGRS.2011.2146786.
- Nur, A., H. Ron, and G. C. Beroza (1993), The nature of the Landers-Mojave earthquake line, *Science*, *261*(5118), 201–203, doi:10.1126/science.261.5118.201.
- Peltzer, G., P. Rosen, F. Rogez, and K. Hudnut (1998), Poroelastic rebound along the Landers 1992 earthquake surface rupture, *J. Geophys. Res.*, *103*(B12), 30,131–30,145, doi:10.1029/98JB02302.
- Peltzer, G., F. Crampé, S. Hensley, and P. Rosen (2001), Transient strain accumulation and fault interaction in the eastern California shear zone, *Geology*, *29*(11), 975–978.
- Pepe, A., A. Bertran Ortiz, P. R. Lundgren, P. A. Rosen, and R. Lanari (2011), The Stripmap-ScanSAR SBAS approach to fill gaps in stripmap deformation time series with ScanSAR data, *IEEE Trans. Geosci. Remote Sens.*, *49*(12), 4788–4804, doi:10.1109/TGRS.2011.2167979.
- Roquemore, G. (1980), Structure, tectonics, and stress field of the Coso Range, Inyo County, California, *J. Geophys. Res.*, *85*(B5), 2434–2440, doi:10.1029/JB085iB05p02434.
- Sauber, J., W. Thatcher, and S. C. Solomon (1986), Geodetic measurement of deformation in the central Mojave Desert, California, *J. Geophys. Res.*, *91*(B12), 12,683–12,693, doi:10.1029/JB091iB12p12683.
- Savage, J. C., and R. O. Burford (1973), Geodetic determination of relative plate motion in central California, *J. Geophys. Res.*, *78*(5), 832–845, doi:10.1029/JB078i005p00832.
- Schmidt, D. A., and R. Bürgmann (2003), Time-dependent land uplift and subsidence in the Santa Clara valley, California, from a large interferometric synthetic aperture radar data set, *J. Geophys. Res.*, *108*(B9), 2416, doi:10.1029/2002JB002267.
- Simons, M., Y. Fialko, and L. Rivera (2002), Coseismic deformation from the 1999 M_w 7.1 Hector Mine, California, earthquake as inferred from InSAR and GPS observations, *Bull. Seismol. Soc. Am.*, *92*(4), 1390–1402, doi:10.1785/0120000933.
- Solt, M., and M. Sneed (2014), Subsidence (2004–09) in and near lakebeds of the Mojave River and Morongo groundwater basins, southwest Mojave Desert, *U.S. Geol. Surv. Sci. Invest. Rep. 2014-5011*, U.S. Geol. Surv., Sacramento, Calif., doi:10.3133/sir20145011.
- Tarayre, H., and D. Massonnet (1996), Atmospheric propagation heterogeneities revealed by ERS-1 interferometry, *Geophys. Res. Lett.*, *23*(9), 989–992, doi:10.1029/96GL00622.
- Tong, X., D. T. Sandwell, and B. Smith-Konter (2013), High-resolution interseismic velocity data along the San Andreas Fault from GPS and InSAR, *J. Geophys. Res. Solid Earth*, *118*(1), 369–389, doi:10.1029/2012JB009442.
- Wadge, G., M. Zhu, R. Holley, I. James, P. Clark, C. Wang, and M. Woodage (2010), Corrections of atmospheric delay effects in radar interferometry using a nested mesoscale atmospheric model, *J. Appl. Geophys.*, *72*(2), 141–149, doi:10.1016/j.jappgeo.2010.08.005.
- Walter, A. W., and C. S. Weaver (1980), Seismicity of the Coso Range, California, *J. Geophys. Res.*, *85*(B5), 2441–2458, doi:10.1029/JB085iB05p02441.
- Wright, T. J., B. Parsons, P. C. England, and E. J. Fielding (2004), InSAR observations of low slip rates on the major faults of western Tibet, *Science*, *305*(5681), 236–239, doi:10.1126/science.1096388.
- Zebker, H. A., P. A. Rosen, and S. Hensley (1997), Atmospheric effects in interferometric synthetic aperture radar surface deformation and topographic maps, *J. Geophys. Res.*, *102*(B4), 7547–7563, doi:10.1029/96JB03804.